A Surface Defect Detection Framework for Glass Bottle Bottom Using Visual Attention Model and Wavelet Transform

Xianen Zhou, Yaonan Wang, Qing Zhu, Jianxu Mao, Changyan Xiao, Xiao Lu, and Hui Zhang

***Abstract*—Glass bottles must be thoroughly inspected before they are used for packaging. However, the vision inspection of bottle bottoms for defects remains a challenging task in quality control due to inaccurate localization, the difficulty in detecting defects in the texture region, and the intrinsically nonuniform brightness across the central panel. To overcome these problems, we propose a surface defect detection framework, which is composed of three main parts. First, a new localization method named entropy rate superpixel circle detection (ERSCD), which combines least-squares circle detection and entropy rate superpixel (ERS) with an improved randomized circle detection, is proposed to accurately obtain the region of interest (ROI) of the bottle bottom. Then, according to the structure-property, the ROI is divided into two measurement regions: central panel region and annular texture region. For the former, a defect detection method named frequency-tuned anisotropic diffusion super-pixel segmentation (FTADSP) that integrates frequency-tuned salient region detection (FT), anisotropic diffusion, and an improved superpixel segmentation is proposed to precisely detect the regions and boundaries of defects. For the latter, a defect detection strategy called wavelet transform multiscale filtering (WTMF) based on a wavelet transform and a multiscale filtering algorithm is proposed to reduce the influence of texture and to improve the robustness to localization error. The proposed framework is tested on four data sets obtained by our designed vision system. The experimental results demonstrate that our framework achieves the best performance compared with many traditional methods.**

***Index Terms*—Anisotropic diffusion, defect detection, saliency detection, superpixel segmentation, wavelet transform.**

Manuscript received January 21, 2019; revised June 14, 2019; accepted August 6, 2019. Date of publication August 13, 2019; date of current version January 17, 2020. This article was supported in part by the National Natural Science Foundation of China under Grant 61733004, Grant 61573134 and Grant 61971071, in part by the National Key R&D Program of China under Grant 2018YFB1308200, in part by the Science and Technology Project of Hunan Province under Grant 2017XK2102, Grant 2018GK2022, and Grant 2018JJ3079, in part by the Scientific Research Fund of Hunan Provincial Education Department under Grant 17C0046, and in part by the Independent Research Subject Funding from the Hunan University State Key Laboratory of Advanced Design and Manufacturing for Vehicle Body. Paper no. TII-19-0205. *(Corresponding author: Jianxu Mao.)*

X. Zhou, Y. Wang, Q. Zhu, J. Mao, and C. Xiao are with the National Engineering Laboratory for Robot Visual Perception and Control Technology, College of Electrical and Information Engineering, Hunan University, Changsha 410082, China (e-mail: zhouxianen@hnu.edu.cn; yaonan@hnu.edu.cn; zhuqing_hnu@163.com; maojianxu@hnu.edu.cn; c.xiao@hnu.edu.cn).

X. Lu is with the College of Engineering and Design, Hunan Normal University, Changsha 410081, China (e-mail: xlu_hnu@163.com).

H. Zhang is with the College of Electrical and Information Engineering, Changsha University of Science and Technology, Changsha 410114, China (e-mail: zhanghuiby@126.com).

Color versions of one or more of the figures in this article are available online at http://ieeexplore.ieee.org.

Digital Object Identifier 10.1109/TII.2019.2935153

I. Introduction

GLASS bottles are easy to mold, relatively inexpensive, highly resistant to internal pressure, and easy to recycle. Thus, glass bottles are widely used in the food and beverage packaging industry, especially for packaging beer and carbonated beverages [1]. However, glass bottles are also susceptible to be damaged during transportation. Once a bottle that contains any defects is filled, many potential hazards, such as product deterioration and bottle explosion, may occur during product storage and transportation. Hence, the quality of each glass bottle must be thoroughly checked.

Manual inspection methods suffer from inherently inconsistent and unreliable detection results because of the subjectiveness and alertness of the inspection worker. As a noncontact sensing technology, machine vision has shown great potential for the quality inspection of industrial products, e.g., quality inspection of weld beads [2], panel displays [3], [4], various metals [5], [6], titanium-coated surfaces [7], solar wafers [8], and pharmaceutical injections [9], [10]. This article focuses on the defect detection of the bottle bottom with a machine vision technique.

Approaches directly related to the bottle bottom are briefly introduced. Most of these methods are composed of two processes: localization and defect detection. Shafait *et al.* [11] obtained the bottle bottom through a generalized Hough transform. Then, the intensity of the bottom region was used to check for defects. Duan *et al.* [12] first employed a histogram of edge points to locate the inspection area since the conventional Hough transform algorithm is slow and the gravity method has large error. Then, two levels of back propagation (BP) neural networks were used to detect defects. There is no special analysis on how to detect the bottle bottom texture region. Ma *et al.* [13]–[15] used the least-squares circle detection (LSCD) and redefined randomized circle detection (RCD) methods to locate the bottom. Then, they

utilized a discrete Fourier transform (DFT) to remove the texture and used threshold segmentation and blob analysis (GTSblob) for the texture region defect detection. To further improve the accuracy of defect detection in the texture region, Zhou *et al.* [16] employed 21HT [17] to obtain the bottle bottom region, and they divided the bottom into three regions for defect detection. They proposed a template-matching-based defect detection algorithm (TM) method that combines template matching with multiscale filtering to detect defects in the texture region. To detect defects in the central panel region, they proposed a region growing euclidean saliency (RGES) method, which integrated the improved superpixel segmentation and geodesic saliency detection algorithms. Moreover, many other surface defect detection methods have also been analyzed to find a suitable solution for inspecting bottle bottoms. For example, anisotropic-diffusion-based (AD) defect detection methods are generally used for low-contrast images [18]–[20]. He *et al.* [20] used the inverse Perona–Malik (P–M) diffusion method (ADblob) for high-speed rails. Many saliency detection methods have recently been used for defect detection, e.g., Bai *et al.* [21] used a saliency detection model based on phase-only Fourier transform for detecting defects in electronic chips. Superpixel-segmentation-based methods are also good choices; for example, Chen *et al.* [22] used a superpixel-segmentation-based method (ERSgraph) for detecting defects in the central panel of the can end.

Although many surface defect detection methods have been reported to date, there are still many problems for bottle bottom inspection, e.g., the inaccurate localization of the bottle bottom, the difficulty in defect detection in the texture region, and the interference of gray value variations across the central panel. To overcome these problems, we propose a novel defect detection framework for glass bottle bottoms. The main contribution of this article is threefold.

1) For the bottle bottom image, it is difficult to realize the high-speed and high-precision positioning with the existed localization methods because of texture interference. The proposed entropy rate superpixel circle detection (ERSCD) strategy first fast obtains a rough location of the bottle bottom using ERS and LSCD on the downsampling image considering that the former can accurately detect the boundaries of a circular object and the latter is a fast circle detection algorithm, then the precise location in the original image is acquired by the proposed improved randomized circle detection (IRCD) algorithm[1].
2) For the texture region, traditional methods usually obtain the annular texture region by the radial development and use the two-dimensional (2-D) structure information of the bottle bottom image to detect defects, which causes that the defect detection result is easily affected by the positioning error. In this article, only the one-dimensional (1-D) information direction is used in each process. Moreover, we propose a new method named wavelet transform multiscale filtering (WTMF)[1] based on a wavelet transform and multiscale filtering because the former can effectively separate the texture from background regions and the latter can suppress noise interference.
3) Gray value variety across the central panel region caused by the thickness differences of bottle bottoms leads to that many defects cannot be detected accurately. To overcome this problem, we propose a fusion method, which integrates the advantages of the saliency detection, anisotropic diffusion, and an improved superpixel segmentation considering that the former two methods enhance all defective regions, and the last algorithm accurately segments defects.

[1]The examples of the proposed IRCD and WTMF are [Online]. Available: https://github.com/zhouxianen/circleDetectionIRCD.git, [Online]. Available: https://github.com/zhouxianen/defDetWTMF.git

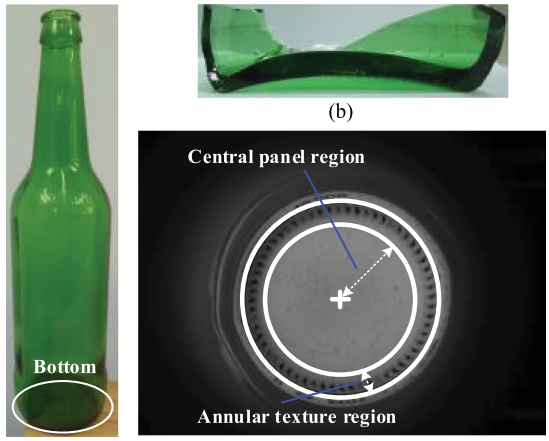

Fig. 1. Structures of the glass bottle bottom. (a) Glass bottle. (b) Tangential section of bottom. (c) Acquired bottom image.

II. Typical Defects and Challenges

As shown in Fig. 1(a), the glass bottle bottom is generally located at the bottom of the bottle. The lower part of the bottle body is a cylindrical shape, and the radius is larger than that of the mouth. The entire bottom shape is similar to a bridge arch; the tangential section of the bottom is shown in Fig. 1(b), and the thickness of the central region is typically thicker than the boundary region. As shown in Fig. 1(c), a glass bottle bottom is usually composed of two regions with different structures: a smooth region and an antiskid texture region. The former named the central panel region is located in the central position. The latter called the annular texture region is used to prevent the glass bottle from sliding.

The defects of glass bottle bottoms are usually classified into four types [16]: opaque foreign objects, such as paperclips and large glass detritus; transparent foreign objects, such as transparent film; contaminants; and self-defects, such as broken bottoms and bubbles. Six images of bottle bottoms with typical defects are shown in Fig. 2. There are generally challenges for the latter three categories, e.g., the boundaries of the contaminants and self-defects are blurred. The contrast between transparent foreign objects and the normal region is particularly low, as shown in Fig. 2(c). Many defects that appear in the texture region are difficult to accurately detect, as shown in the lower right corner of Fig. 2(a). Moreover, the gray values of the panel region change over a wide range for different bottle bottom

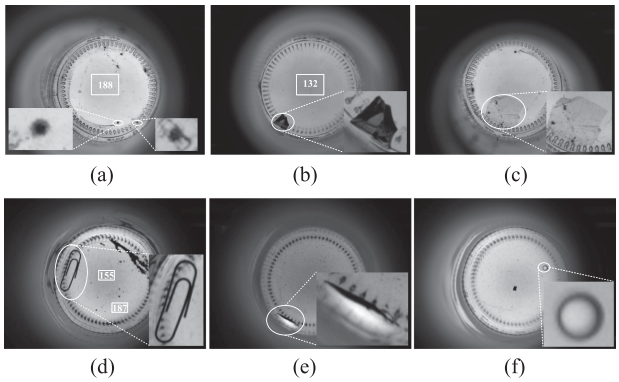

Fig. 2. Typical defects of glass bottle bottoms. (a) Smudginess. (b) Glass detritus. (c) Transparent film. (d) Paperclip. (e) Damaged bottom. (f) Bubble.

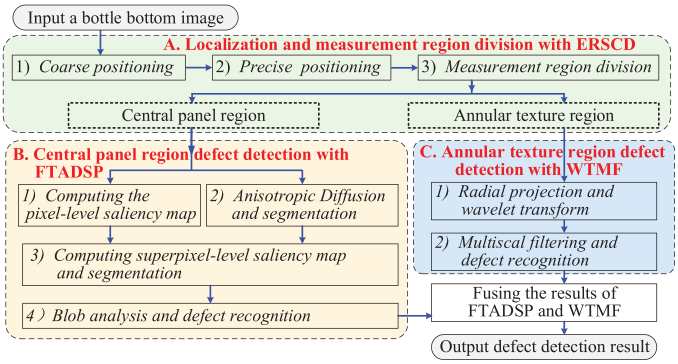

Fig. 3. Proposed defect detection framework for the bottle bottom image.

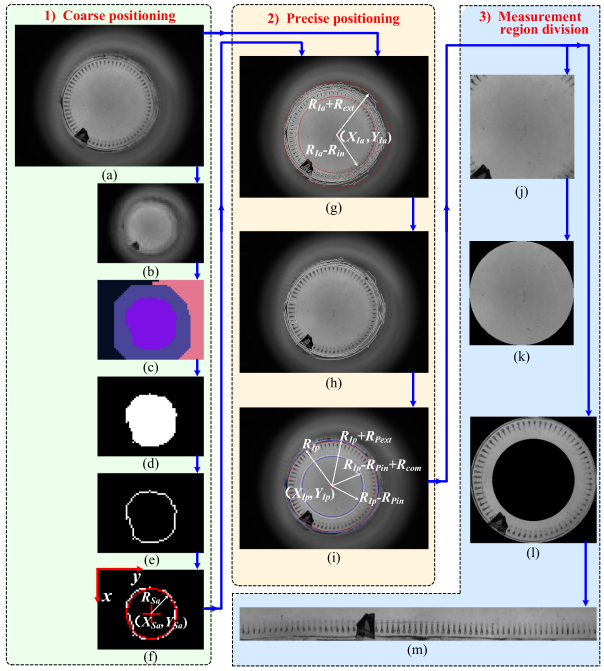

Fig. 4. Pipeline of the proposed ERSCD localization method. (a) A entire bottle bottom image. (b) The resized image. (c)–(f) are the ERS segmentation, objective circular region, objective region boundary, and approximate center in the resized image, respectively. (g) and (h) are the canny edges and objective edges in a constrained region in the original image. (i) The precise center of the bottle bottom with the proposed IRCD algorithm. (j) Rectangular-shaped central panel region. (k) Central panel region obtained by removing the four corner texture regions. (l) Ring-shaped circular texture. (m) Annular texture region unwrapping, which is called the annular texture region for short.

images because of the differences in the bottom thickness, as shown by the white rectangular region in Fig. 2(a), (b), and (d). Note that images in Figs. 1(c) and 2 are acquired by our designed vision inspection system, which is introduced in Section IV.

III. Proposed Method

The entire flowchart of the proposed framework mainly consists of ERSCD, frequency-tuned anisotropic diffusion superpixel segmentation (FTADSP), and WTMF, as shown in Fig. 3. Followed, the details of these proposed methods are described.

A. Localization and Measurement Region Division With ERSCD

The bottle bottom does not present at a fixed position in the obtained image due to the mechanical vibration from the conveyor motion. Therefore, it is necessary to localize the bottom for each tested bottle. To achieve high positioning precision and high efficiency, a new localization strategy named ERSCD inspired by Chen's localization method [22] is proposed. It is composed of the coarse positioning, precise positioning, and measurement region division, as shown in Fig. 4, where the IRCD in the second step is also our contribution.

1) Coarse Positioning: As shown in Fig. 4(a)–(f), the low-resolution image of the input image, where the length-width ratio remains unchanged, is first obtained by downsampling to accelerate the execution speed of coarse positioning as

$$S_{\text{small}} = s_r * S_{\text{input}} \tag{1}$$

where S_{input} and S_{small} denote the sizes of the input and resized image. s_r is the lessen ratio, $0 < s_r \leq 1$. Then, the ERS segmentation algorithm [23] is employed to divide this resized image into many regions, and the quasicircular superpixel with the maximum average is selected as the objective region. Subsequently, the boundary of this circular object is fed into the LSCD algorithm [24] to calculate the approximate center coordinates and radius in the resized image. Finally, the corresponding results in the original size image is obtained by

$$X_{Ia} = X_{Sa}/s_r \tag{2}$$

$$Y_{Ia} = Y_{Sa}/s_r \tag{3}$$

$$R_{Ia} = R_{Sa}/s_r \tag{4}$$

where X_{Sa}, Y_{Sa}, and R_{Sa} represent the approximate center coordinates and radius of the bottle bottom in the down-sampling image, and X_{Ia}, Y_{Ia}, and R_{Ia} are the approximate center coordinates and radius of the bottle bottom in the original input image, respectively.

2) Precise Positioning: As shown in Fig. 4(g)–(i), to find the desired edges of the bottom, we first obtain the Canny edges in

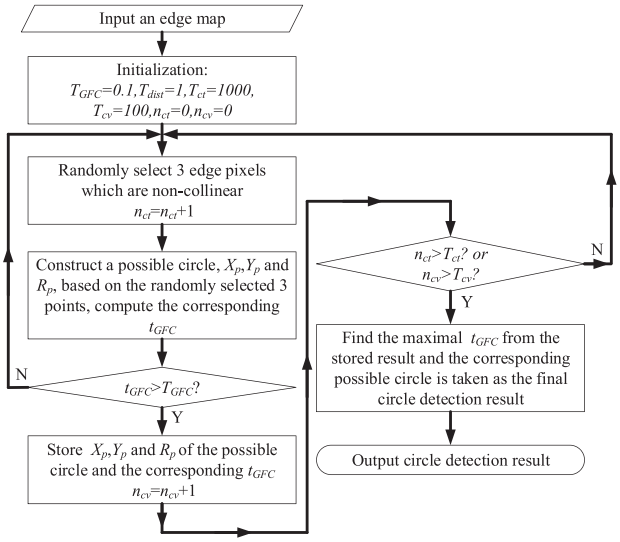

Fig. 5. Flowchart of the proposed IRCD algorithm. The parameters of a possible circle including center x and y coordinates and radius are calculated by three edge pixels, which are noncollinear. T_{ct}, T_{cv}, and T_{GFC} are three manually set thresholds.

a constrained region satisfying the requirement

$$R_{Ia} - R_{\text{in}} \le \text{sqrt}((x - X_{Ia})^2 + (y - Y_{Ia})^2) \le R_{Ia} + R_{\text{ext}} \tag{5}$$

where R_{in} and R_{ext} are two thresholds set by the prior shape constraint, sqrt() denotes the square root function, and x and y are coordinates of a pixel in the image. Then, the edges whose lengths are smaller than a threshold are removed. Finally, the remained edges are sampled with a fixed step L_{se} to reduce the computational load and then fed into the proposed IRCD method to calculate the precise positioning result. IRCD is an improved version of RCD [25], it is used for single circle detection and has fewer parameters needed to be manually set than RCD. For evaluating the degree of fitting of each possible circle, we define a measurement criterion

$$t_{\text{GFC}} = n_{cv}/n_{ct} \tag{6}$$

where n_{ct} denotes the number of total edge pixels and n_{cv} represents the number of edge pixels lies on a possible circle. To distinguish whether an edge pixel lies on a possible circle, a distance d_e is defined as

$$d_e = \left| \sqrt{(x - X_p)^2 + (y - Y_p)^2} - R_p \right| \tag{7}$$

where X_p, Y_p, and R_p are the center coordinates and radius of a possible circle. If an edge pixel meets to the requirement $d_e < T_{\text{dist}}$, it is considered to lie on the possible circle. T_{dist} is a given threshold, and it is generally a small integer, such as 1 or 2. The flowchart of the proposed IRCD is presented in Fig. 5.

3) Measurement Region Division: Depending on the structure-property of the bottle bottom, the region of interest (ROI) is divided into the central panel region and annular texture region, as shown in Fig. 4(i), their coordinates respectively meet the followed requirements:

$$\text{sqrt}((x - X_{Ip})^2 + (y - Y_{Ip})^2) \le R_{Ip} - R_{P\text{in}} + R_{\text{com}} \tag{8}$$

$$R_{Ip} - R_{P\text{in}} \le \text{sqrt}((x - X_{Ip})^2 + (y - Y_{Ip})^2) \le R_{Ip} + R_{\text{Pext}} \tag{9}$$

where X_{Ip}, Y_{Ip}, and R_{Ip} are the precise center coordinates and radius of the bottle bottom, and $R_{P\text{in}}$, R_{com}, and R_{Pext} are three thresholds easily determined by the prior size knowledge.

Consider that the original annular texture region is a ring-shaped image, which is not convenient for processing. Hence, we transform it into a rectangular image named annular texture region, as shown in Fig. 4(m), with a radial development approach [22].

B. Central Panel Region Defect Detection With FTADSP

For the central panel region, to accurately detect the entire regions of defects and obtain the correctly boundaries, especially for the defects with the small size and low-contrast, we proposed the strategy FTADSP composed of saliency detection, anisotropic diffusion, and superpixel segmentation, which is inspired by the similar techniques [16], [20]–[22]. First, consider that all kinds of defects have a common property, i.e., they usually cover a closed region to the homogeneous grayscales, which is similar with the definition of the superpixel [22]. But if defects are determined by the gray-levels, many defects with low-contrast cannot be detected. To cover this problem, defects can be seen as many similar superpixels and selected by their saliency values [16]. Because the inner regions of defects are usually unpredictable and sparse, they can be formulated as salient regions [21], with the inspiration of human visual attention model [26], [27]. Moreover, depending on an anisotropic diffusion and image differencing operation, defect boundaries can be enhanced and many noised can be suppressed [20]. However, many inner regions of defects cannot be detected correctly. Therefore, to precisely detect the entire regions of defects, we further obtain the union result of the AD method and defect detection result obtained by the saliency detection and superpixel segmentation. The flowchart of FTADSP is shown in Fig. 6.

1) Computing Pixel-Level Saliency Map: The defective regions in a bottle bottom image generally stand out with respect to their neighborhood. As a high-efficacy and easy-to-implement method, the original frequency-tuned salient region detection (FT) is usually used for salient object segmentation for color images [28]. This article applies the frequency-tuned salient region detection (FT) algorithm to enhance the contrast between all suspected regions and the background region. Consider that the bottle bottom image is grayscale, we compute the saliency value of each pixel with respect to its neighborhood in terms of its lightness property by taking the entire image as the neighborhood, i.e.,

$$I_S(x, y) = |I_u - I_g(x, y)| \tag{10}$$

where I_S, I_u, and I_g denote the saliency map, arithmetic mean pixel value of the image and the Gaussian blurred image, respectively, and $|*|$ represents absolute value operation.

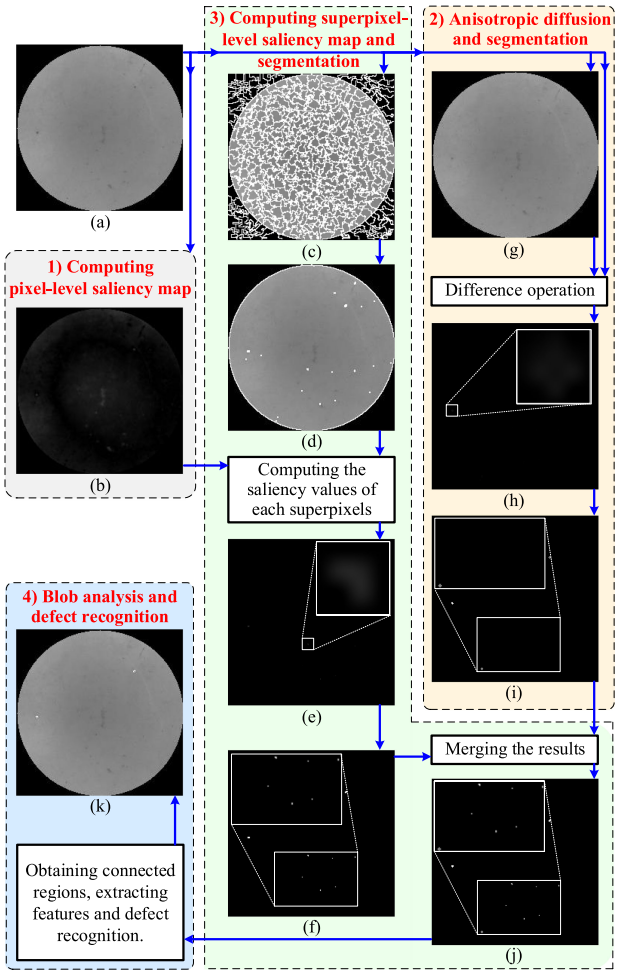

Fig. 6. Flowchart of the proposed FTADSP method for the central panel region. Defects are marked by the white regions in figure (k). (a) Central panel region. (b) FT saliency map. (c) ERS segmentation. (d) Region growing. (e) Superpixel-level saliency map. (f) Segmentation result of the superpixel-level saliency map. (g) Anisotropic diffusion result. (h) Difference image. (i) Segmentation result. (j) The union set. (k) Defect detection result.

2) Anisotropic Diffusion and Segmentation: To detect as many suspected defects as possible, a nonlinear anisotropic diffusion operation [20] that can smooth all suspected defects and simultaneously preserve the original scale of the background region is employed. The pipeline is composed of three steps: nonlinear diffusion, difference operation, and global threshold binarization, as shown in Fig. 6(g), (h), and (i). For the difference image, those pixels with gray values that are larger than the threshold T_{AD} are considered to be the suspected defects.

3) Computing Superpixel-Level Saliency Map and Segmentation: As shown in Fig. 6(c)–(j), the input bottom image is first divided into K superpixels by the ERS algorithm [23], which poses the superpixel segmentation problem as a maximization problem on a graph and presents a novel objective function on the graph topology, where K is a key parameter of ERS that needs to be set manually. There is a problem that the background region cannot be clustered into a whole, as shown in Fig. 6(c), when only resorting to the ERS segmentation. Therefore, we combine ERS with a region growing algorithm to obtain a compact segmentation result where each segment is more likely to be a whole background or a complete object. For the region growing algorithm, the initial seed superpixel of a new class is selected in order from the unlabeled superpixels. The superpixel close to the current growing region will be merged into the current class if the grayscale difference of these two regions is smaller than a threshold T_{RG}, where the difference is measured by the Euclidean distance. The process repeats until the aforementioned condition is not satisfied. The final superpixel region growing result and pixel-level saliency map are fused similar to the superpixel segmentation and grabcut-based salient object segmentation (SSG) method [29]. The saliency value of the ith superpixel is calculated by

$$\mathrm{S}'_{\mathrm{R_i}} = \frac{1}{|R_i|}\sum_{j}^{|R_i|} S_{R_{ij}} \tag{11}$$

where R_i and $|R_i|$ represent the ith superpixel region and the pixel number of the corresponding region. S_{Rij} denotes the jth pixel in the ith superpixel region obtained by region growing. Moreover, consider that the background region typically has the maximum size. We further suppress noise interference by

$$S_{R_i} = |S'_{R_i} - S_{R_{\max}}|. \tag{12}$$

Here, $S_{R\max}$ represents the saliency value of the superpixel region with the maximum size in the central panel region.

Moreover, consider that the saliency values of defective regions are generally higher than the values of normal regions. Hence, it is reasonable to distinguish defects and normal regions according to the following rule: if the saliency value of a region is larger than a certain threshold, i.e., $S_{Ri} > T_{sm}$, then the region is considered as a desired defect, where T_{sm} is a threshold that is set according to the prior knowledge. Finally, many suspected defects can be acquired by this the rule described above, as shown in Fig. 6(f).

4) Blob Analysis and Defect Recognition: The union set of the superpixel-level saliency map and difference image are first obtained, as shown in Fig. 6(j). Then, all connected regions are obtained, and the size of each connected region is counted. Those regions with areas larger than a threshold T_{area} are distinguished as the final desired defects, as shown by the small white regions in Fig. 6(k).

C. Annular Texture Region Defect Detection With WTMF

Consider that the wavelet transform can effectively separate the signals with different frequencies, while multiscale filtering can suppress noise interference. We propose a strategy called WTMF that fuses these two methods for the annular texture region defect detection. The flowchart is illustrated in Fig. 7.

1) Projection and Wavelet Transform: The projection of the annular texture region along the vertical direction, denoted as S_{AT}, is first obtained by computing the mean value of each column pixel as

$$S_{AT}(y) = \frac{1}{H_{AT}}\sum_{x=1}^{H_{AT}} I_{AT}(x,y) \tag{13}$$

where H_{AT} is the height of the annular region image I_{AT}. Then, to suppress the impact of the texture structure on defect detec-

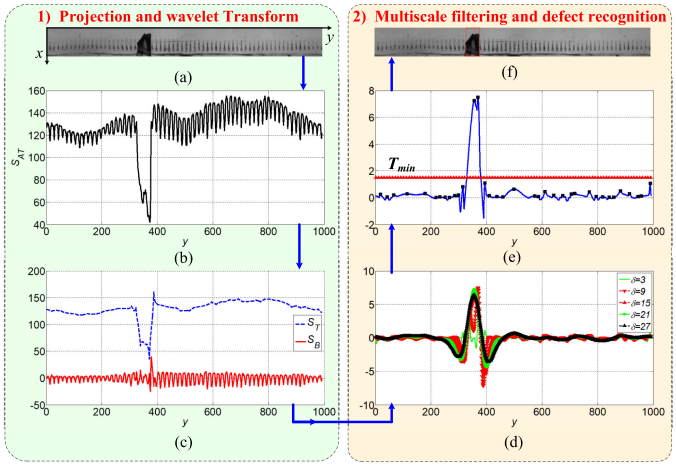

Fig. 7. Process of the proposed WTMF strategy for the annular texture region. Defect is marked by the red rectangle in figure (f). (a) The tested annular texture region. (b) Projection signal in vertical direction. (c) Basewave signal and texture signal obtained by wavelet transform. (d) Multiscale filtering results. (e) Maxima of the filtering results. (f) Defect detection result.

tion, the 1-D projection signal S_{AT} is processed by a wavelet transform because the 1-D signal S_{AT} is the superposition of two subsignals: base-wave signal and texture signal, which are represented by $S_B(y)$ and $S_T(y)$, respectively. The former is a signal with a low frequency, while the latter is a high-frequency signal. Hence, $S_B(y)$ and $S_T(y)$ can be separated by a wavelet transform. In this article, the maximum decomposition level is set to 4. The original input signal S_{AT} is decomposed into the sum of a series of signals

$$cA0 = S_{AT} = sA4 + sD4 + sD3 + sD2 + sD1 \tag{14}$$

where $sA4$, $sD4$, $sD3$, $sD2$, and $sD1$ are the wavelet reconstruct signals of the corresponding single branch. The fourth layer approximation signal $sA4$ shows the basic contour of the projection signal, while the sum of the detail signals $cD1$, $cD2$, $cD3$, and $cD4$ contain the texture structure information of the bottle bottom, i.e., $S_B(y) = sA4$ and

$$S_T(y) = sD4 + sD3 + sD2 + sD1 \tag{15}$$

as shown in Fig. 7(a)–(c).

2) Multiscale Filtering and Defect Recognition: As shown in Fig. 7(e) and (f), defective regions generally appear as valleys or ridges on the base-wave signal $S_B(y)$ obtained by the wavelet decomposition. Additionally, the widths of the defects are proportional to those of the valleys and ridges. On this basis, we proposed a multiscale filtering method for locating defective regions. According to a traditional multiscale line segmentation algorithm [30], we know that the Gaussian-, step-edge-, and bar-like profiles can be estimated using the local extrema of γ-parameterized normalized derivatives [31]. In this article, to ensure a positive response for defective regions with low grayscale values, the base-wave signal is first convolved with a series of second-order Gaussian kernels with different scales as

$$r(y,\delta) = \delta^{\gamma} \cdot S_B(y) * g''(y,\delta) \tag{16}$$

with $\gamma = 3/2$. The positions and widths of defects can be measured with the maxima of the series of responses as

$$\mathrm{D}(y) = \max_{\delta_{\min} \le \delta \le \delta_{\max}} \{r(y,\delta)\} \tag{17}$$

where $\delta_{\min}$ and $\delta_{\max}$ correspond to half of the minimum and maximum defects in the obtained bottle bottom images. The ridges in the 1-D signal $D(y)$ generally correspond to the defective regions or the boundary regions of defects. Hence, a threshold on $D(y)$, $T_{\min}$, is sufficient for distinguishing the qualified and unqualified annular texture regions.

IV. Experiments

In this section, the designed vision system and the implementation of the proposed framework are first introduced. Meanwhile, four test data sets used in the followed experiments are created and described. Then, the measures used to verify the effectiveness of the proposed framework, and parameters sensitivity analysis are presented. Besides, the performances of the proposed ERSCD, FTADSP, WTMF, and entire framework are individually evaluated on the calibrated data sets.

A. System Design and Implementation

To acquire a clear image of the bottle bottom, we designed a machine vision apparatus, as shown in Fig. 8, which is composed of three main parts: 1) electromechanical device, 2) processing module, and 3) imaging system. The last component consists of a camera, planar light source, and photosensor, and is mainly used to process the acquired image. The green glass bottles of the TSINGTAO beer, as shown in Fig 1(a), taken as tested bottles, where the bottom diameter of 75 mm, are employed for demonstration, and a monochrome camera with a resolution of 648×483 can satisfy the inspection requirements. The light source is fixed below the bottom inspection station. To prevent water and foreign objects from falling onto the light source, an inclined protective glass is installed above it. To avoid ambient light, the camera is installed in a closed box above the light source and looks down at the bottle bottom through the bottleneck opening of the bottle. By this setup, no matter which side (the outer or inner surface of the testing bottle bottom) defects appear on, defective regions can be clearly imaged. Moreover, the quality of the inner surface of the bottle bottom is much more important than that of the outer surface because the food and beverage are packaged in the bottle. If foreign matters on the inner surface of the bottle bottom are mixed into the food and beverage that will endanger consumers' health.

The designed imaging system can get a good shot with the aid of an optoelectronic switch installed at the central line position of the camera and light source, as shown in Fig. 8(c). As a test bottle is transmitted to the position of the optoelectronic switch. A valid signal is generated by the optoelectronic sensor. Programmable logic controller (PLC) receives the signal and immediately generates two trigger signals used for turning on the planar light source and triggering the camera to capture the bottom image.

To verify our framework, beer glass bottles from the practical industrial field are tested on the designed test system, as shown in

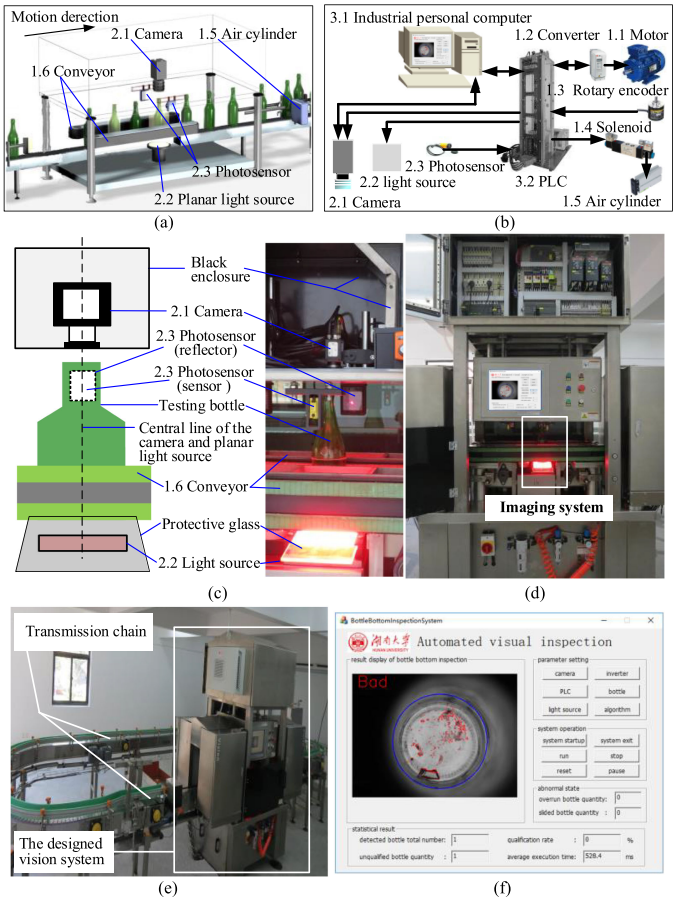

Fig. 8. Schematic and real photographs of the developed vision system. (a) Structure of the vision system. (b) Electrical control system. (c) The front view and real photo of imaging system. (d) The designed vision system. (e) Real photo of the entire test system. (f) Software user interface.

Fig. 8(e). A video that our framework is tested on the designed system is available[2]. The inspection software is implemented with VS2012, where the Open Source Computer Vision Library (OpenCV) and wavelet toolbox of MATLAB are needed. The designed user interface is shown in Fig. 8(f), where parameter setting and system operation are distributed on the upper-right part corner. Other parts present the final image and statistical results of defect detection.

We use the designed system to acquire the bottle bottom images and create four data sets to evaluate the proposed methods. The first data set contains 29 images with typical defects for estimating the performances of FTADSP and WTMF. The second data set includes 11 images that are selected from the previous data set for evaluating the performance of ERSCD and for measuring the influence of a location error on the annular region defect detection. The other data set consists of 1230 images, including 253 normal images without any defects, where there are 343 and 736 defect-free region subimages of the central panel and annular texture regions, respectively. The last data set, which contains 1230 images, is used for measuring the performance of the entire framework. The resolutions of these bottle bottom images are 648×483 pixels.

All the proposed framework is programmed with C++ language except that WTMF is implemented using MATLAB language because using MATLAB is more convenient and easier than employing C++ to verify the proposed WTMF methods considering that there are more than 10 wavelet functions packaged in the wavelet toolbox of MATLAB. All the followed experiments are implemented on the same computer equipped with an Intel Core i5-4210U (1.7–2.4G) CPU, 6 GB of RAM, and the Windows 10 64-bit operating system. The original images, calibrated data sets and experimental results are available[3].

B. Measures and Parameter Sensitivity Analysis

To validate the localization methods, the center deviation E_X, E_Y, radius mismatch E_R, and overall positioning error E_d are defined as

$$E_X = |X_L - X_m| \tag{18}$$

$$E_Y = |Y_L - Y_m| \tag{19}$$

$$E_R = |R_L - R_m| \tag{20}$$

$$E_d = \sqrt{{E_X}^2 + {E_Y}^2 + {E_R}^2} \tag{21}$$

where X_m, Y_m, and R_m denote the manually calibrated results, while X_L, Y_L, and R_L are the results of the localization methods. To fairly compare the performances of all compared defect detection methods, three popular indicators including precision (P_r), recall (R_e), and F-measure (F_β) are employed [16]. Note that the pixel, separate measurement region subimage, or entire bottom image are taken as the basic unit to compute these measures. Moreover, the consumed time (T_{cs}) of each method is also measured.

The proposed framework has eight key parameters including T_{ct}, L_{se}, K, T_{RG}, T_{area}, T_{sm}, T_{AD}, and $T_{\min}$ that are set independently and have little influence on each other. These parameters are set according to the prior knowledge and testing experiments, and it is easy to obtain their appropriate values. Moreover, for the same type of the bottle bottom, the parameters need to be set only once because the parameters have strong robustness. We do not need to adjust the parameters for each input image.

T_{ct} and L_{se} belong to ERSCD, and their values are selected by minimizing E_d. The localization error and consumed time curves of T_{ct} and L_{se} are shown in Fig. 9(a)–(d). It is clear that the larger the value of T_{ct}, the higher the positioning accuracy, and the longer the execution time. As L_{se} increases, the consumed time decreases dramatically while the positioning errors are always kept to small values. The results reveal a fact that downsampling the edge points can greatly improve the execution speed of the IRCD algorithm and the error of localization almost

[2][Online]. Available: https://pan.baidu.com/s/1n9K0sL3LN_hkNyyfRdUXRw, extraction code: 5yzz

[3][Online]. Available: https://pan.baidu.com/s/1bp0pUWposO5LX0EGtKPQAw

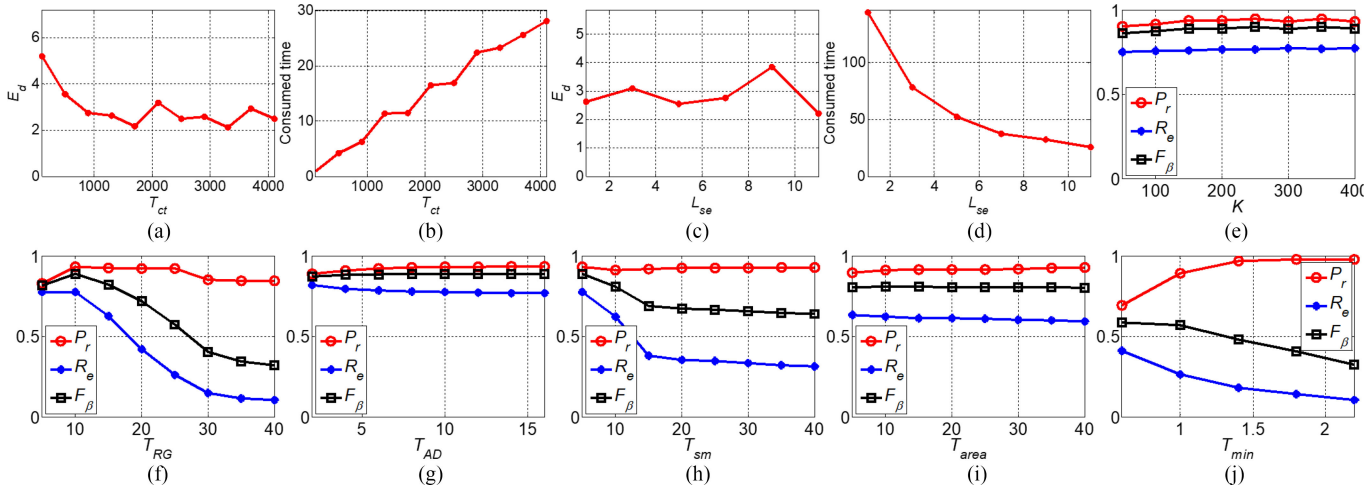

Fig. 9. Parameter sensitivity analysis of the proposed framework.

keeps the same. WTMF strategy has only one parameter $T_{\min}$. Other parameters belong to FTADSP. Parameter sensitivities of the FTADSP and WTMF are respectively analyzed on the central panel region and annular texture region of 29 bottle bottom images. The standard parameter settings are $K = 400$, $T_{RG} = 10$, $T_{AD} = 10$, $T_{\text{area}} = 4$, $T_{sm} = 10$, and $T_{\min} = 1$. For WTMF, the wave function is Coiflets (coif1). When the value of one parameter changes in a certain range, those of other parameters keep unchanged. The variation curves are given in Fig. 9(e)–(j). For T_{RG}, when it is less than a certain threshold, the smaller its value is, the smaller that of R_e is, since that many small defect-free regions, which cannot be merged into the greater background region, mistakenly detected as defects. When T_{RG} is larger than the threshold, R_e decreases as it increases because the greater T_{RG} usually corresponds to larger sizes of superpixels, which leads to that many small defects cannot be detected. For T_{sm} and $T_{\min}$, small values of those usually correspond to large values of R_e because the parts with large values of T_{sm} and $T_{\min}$ are considered to be the desired defects.

In a word, T_{RG}, T_{sm}, and $T_{\min}$ have a great influence on the final results of defect detection. The values of these three parameters can be easily determined based on the prior knowledge of the defects. Conversely, the influences of K, T_{AD}, and T_{area} on the evaluation indices are slight and similar.

TABLE I
COMPARATIVE PERFORMANCES OF MANY POPULAR LOCALIZATION METHODS

method	E_X	E_Y	E_R	E_d	T_{cs} (ms)
ERSIRCD	**1.7**	2.9	3.9	3.7	15.11
ERSRCD	17.9	10.0	16.9	22.6	5.52
ERSHTCD	2.2	2.5	3.5	3.7	86.84
ERSLSCD	4.2	6.3	**2.3**	8.1	**0.03**
Chen's method [22]	2.1	**1.3**	6.2	**2.7**	4447.91
21HT [17]	2.3	2.4	4.6	3.8	70.36

The bold values denote the best results.

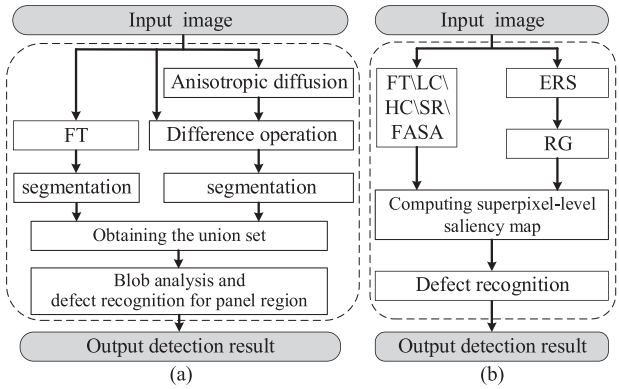

Fig. 10. Flowcharts of FTAD and SMSP. (a) FTAD. (b) SMSP.

C. Performance of ERSCD

To evaluate the errors of ERSCD, the boundaries of the ROIs of 11 bottle bottom images are first manually marked. Then, the center and radius are obtained with the traditional Hough transform circle detection algorithm [17].

In the following, we compare similar combination strategies and many other localization algorithms with the proposed method on these 11 images. In the proposed ERSCD framework, the IRCD algorithm can be replaced by other popular circle detection methods, such as LSCD [24], HTCD [17], and RCD [25]. On the one hand, these combinations are compared with each other to validate the proposed IRCD. On the other hand, 21HT [32] and the Chen's method [22] are also compared with the proposed framework since they can also be directly used for positioning the bottle bottom. The former is an optimized HTCD algorithm that has been implemented by many popular software or image processing toolkits, such as MATLAB and OpenCV. The latter is a new single circular object localization method and can achieve high localization precision. For each method, we select the best parameter settings. The parameter settings of our localization method ERSIRCD are $T_{ct} = 1700$ and $L_{se} = 10$. The comparative performances are reported in Table I.

We find that the Chen's method achieves the highest localization precision. However, it is the slowest algorithm because this method is based on ERS without any speed-up strategy, while ERS employs a greedy search method. ERSLSCD is the fastest method because we have downsampled the input image to reduce computation; meanwhile, LSCD can directly obtain the circle parameters by solving a linear system of equations. However, the corresponding localization error is the largest one except for that of ERSRCD. Additionally, the performances, including the localization and time consumption, of ERSHTCD and 21HT are clearly inferior to that of ERSIRCD. Moreover, our method has only a small localization error, i.e., $E_d = 3.7$, which is only 1.0 larger than that of the Chen's method. But the speed of our approach is about 300 times that of latter. Generally, it has the highest computational efficiency except for the ERSLSCD and ERSRCD.

D. Performance of FTADSP

Many methods are compared with the proposed FTADSP on 29 central panel region images. First, consider that FTADSP consists of saliency detection, anisotropic diffusion, and superpixel segmentation. Hence, the SMSP and FTAD approaches, as shown in Fig. 10, are compared because they are very similar to our method. The former is based on saliency detection and superpixel segmentation, and in the framework of SMSP, many high-efficacy saliency detection algorithms, including FT [28], luminance-based contrast saliency detection (LC) [33], histogram-based contrast saliency detection (HC) [34], spectral residual-based saliency detection (SR) [35], and fast, accurate, size-aware salient object detection (FASA) [36], can also be employed, and the combinations that combine these methods with superpixel segmentation are respectively abbreviated as frequency-tuned super-pixel segmentation (FTSP), luminance contrast super-pixel segmentation (LCSP), histogram contrast super-pixel segmentation (HCSP), spectral residual super-pixel segmentation (SRSP), and fast, accurate, size-aware super-pixel segmentation (FASASP). Moreover, four other approaches, namely, ERSgraph [22], GTSblob [15], ADblob [20], and RGES [16], are also compared with FTADSP. The parameter settings of FTADSP are $K = 400$, $T_{RG} = 10$, $T_{sm} = 10$, and $T_{\text{area}} = 4$. Some visual results are shown in Fig. 11. It is obvious that the great majority of defects have been detected accurately. The comparative performances are reported in Table II.

It is clear that the measures of FTADSP are higher than those of other methods, and the time consumed by our method is approximately equivalent to those of the SMSP and ERSgraph methods. Although GTSblob is the fastest method, its recall and F-measure are clearly lower than those of the other methods. Moreover, we also discover that SMSP methods, except SRSP and FASASP, can considerably improve the precision, recall, and F-measure compared with the other methods. SR downsamples the input image, which leads to some small defects being unable to be detected. FASA depends on the prior knowledge of the positions of defects. However, defects may appear at any location in the bottle bottom. In other words, for defect detection, the location prior is invalid. FTAD has high

TABLE II
COMPARATIVE PERFORMANCES OF DEFECTION DETECTION TEST IN THE CENTRAL PANEL REGION OF BOTTLE BOTTOM

method	$P_r(\%)$	$R_e(\%)$	$F_\beta(\%)$	T_{cs} (ms)
FTADSP	93.16	77.46	**88.97**	465.04
FTAD	90.62	31.84	63.54	25.35
FTSP	**93.24**	77.02	88.89	448.05
HCSP	90.36	**78.88**	87.40	441.89
LCSP	90.04	78.85	87.16	451.23
SRSP	83.77	20.74	47.83	441.46
FASASP	48.14	65.77	47.42	439.25
ERSgraph [22]	82.99	25.44	54.46	460.79
GTSblob [15]	75.14	19.57	44.17	**4.83**
ADblob [20]	80.12	13.53	37.38	9.87
RGES [16]	92.60	71.22	86.58	45.75

efficacy, precision, and F-measure, but the recall value is clearly lower than that of other methods combined with the superpixel segmentation algorithm. The recall of ADblob is lower than that of any other method since only the boundary regions of defects are highlighted by the inverse P–M diffusion algorithm. The precision and F-measure of RGES are similar to those of FTSP and FTADSP since the majority of defects are also highlighted by the Euclidean distance transform and FT saliency detection methods, whereas the recall of RGES is clearly lower than those of the latter two methods because many inconspicuous defects, especially defects with diffusion boundaries, cannot be accurately detected by the region growing algorithm. FTADSP also has a drawback that it is a time-consumed method because of three reasons. First, its programming codes are implemented without using optimization and hardware-accelerate technique. Second, it is tested on a computer with very low configuration. Finally, it uses a time-consumed method, ERS superpixel segmentation algorithm. To speed-up FTADSP, we can try to improve ERS algorithm, replace it with a faster method to further speed-up the proposed framework, and optimize the codes in future work.

Generally, we can conclude that the proposed FTADSP does integrate the merits of ADblob, SMSP, and SMAD; hence, it is superior to any one of the three methods and many traditional methods. Note that although the data set used for testing is the same, the results of GTSblob, ADblob, and RGES in this article are different than those of the three methods in the literature [16] for two main reasons. First, Zhou *et al.* [16] calculated the evaluation indices by taking each connected region as the basic unit, while this article computes the measures by taking each pixel as the basic unit. Moreover, this article divides the bottom into two measurement regions, while the bottom is separated into three measurement regions in the literature [16], which can locate the texture region more accurately.

E. Performance of WTMF

The proposed WTMF with different wavelet functions, DFT-based method [15] and TM-based method [16] are tested on 29 annular texture region images. For WTMF methods, six wavelet families, including coiflets (coif1), reverse biorthogonal (rbio6.8), biorthogonal (bior6.8), symlets (sym2), discrete approximation of meyer (dmey), and daubechies (db1), are tested.

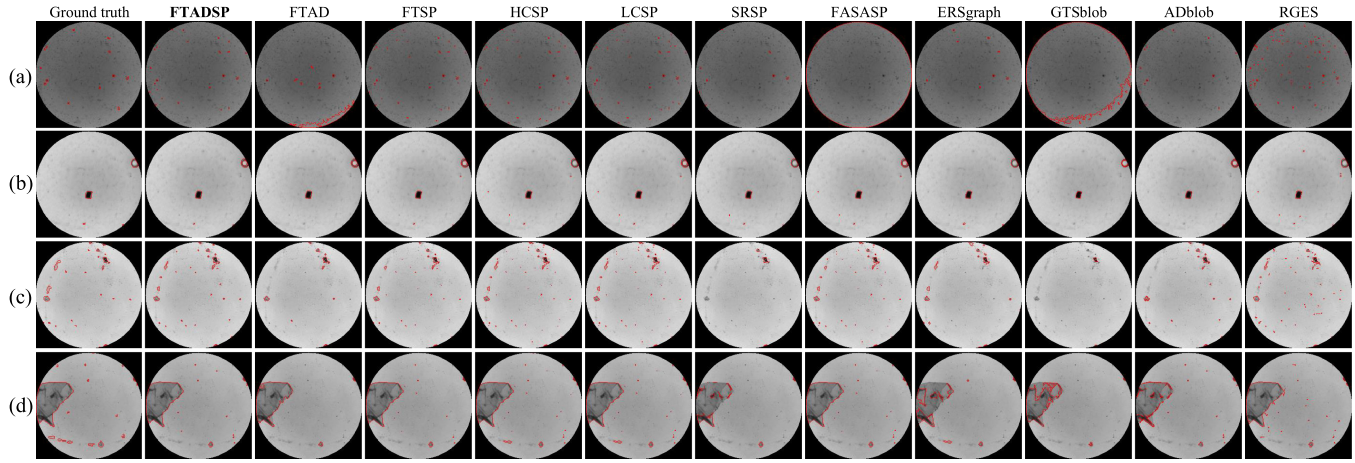

Fig. 11. Comparison results from different methods for central panel region.

TABLE III
COMPARATIVE PERFORMANCES OF DEFECTION DETECTION TEST IN THE ANNULAR TEXTURE REGION OF BOTTLE BOTTOM

method	$P_r(\%)$	$R_e(\%)$	$F_\beta(\%)$	T_{cs} (ms)	code
coif1MF	**89.26**	26.39	**56.91**	58.0	MATLAB
rbio6.8MF	88.66	26.31	56.28	64.0	MATLAB
bior6.8MF	89.04	26.24	56.27	82.0	MATLAB
sym2MF	89.25	26.38	56.81	53.0	MATLAB
dmeyMF	86.75	26.37	56.07	69.5	MATLAB
db1MF	86.22	26.34	55.30	54.1	MATLAB
DFT [15]	61.66	24.87	45.95	**11.7**	C++
TM [16]	46.34	**43.97**	40.60	13.83	C++

And set $T_{\min} = 1$. The comparative performances and some typical results are presented in Table III and Fig. 12, respectively.

As shown, although the DFT-based method is faster than the other methods, the precision and F-measure of WTMF approaches are clearly better than those of the other two methods, where the "coif1MF" method can achieve the best performance on the testing data set. This phenomenon occurs because the base-wave signal and texture signal can be effectively divided with the wavelet-transform-based methods. DFT and TM can also suppress the influence of regular texture on defect detection, while these two methods are easily influenced by the texture structure features and localization error of the tested texture region. Conversely, the two factors only have a slight influence for the WTMF methods. Unfortunately, there is also a shortcoming for WTMF methods, i.e., defects with high grayscale levels cannot be accurately detected as an entire region. More accurately, only the left and right boundaries of the defect are found by the WTMF methods, taking the broken glass and bubble as examples, as shown in Fig. 12(a) and (b).

Moreover, to further verify the conclusion that WTMF methods have much stronger robustness to the localization error than DFT and TM, the annular texture regions from 11 bottom images with different localization errors are first obtained. Consider that the real localization errors in the y-axis direction E_Y are generally larger those along the x-axis E_X since the tested glass bottle is clamped by two conveyors, as shown in Fig. 8(c), which makes the position of the tested bottle in the x direction

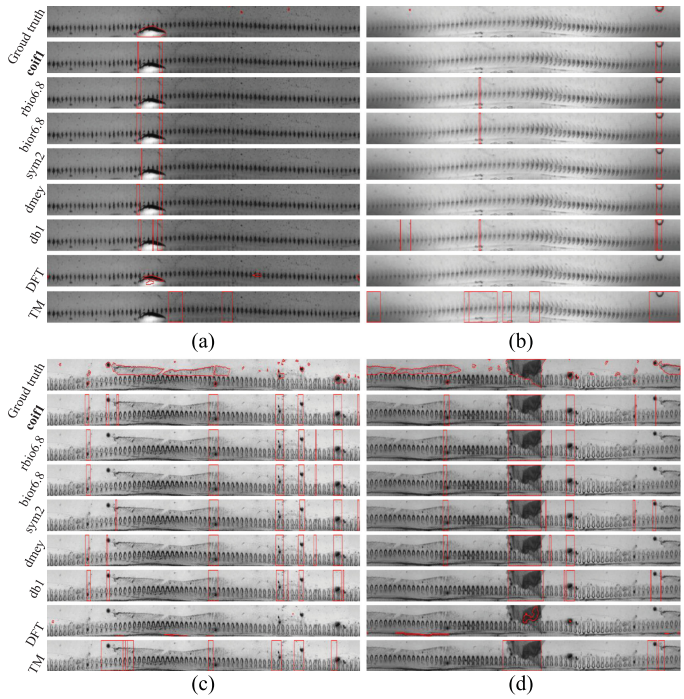

Fig. 12. Comparison results from different methods for annular texture region.

relatively fixed, while the bottle may be inclined and sliding, leading to substantial error in the y direction. Therefore, we assume that $E_X = 0$ and that E_Y changes with a fixed step. Then, the coif1MF, DFT, and TM methods are separately tested. The measured curves are reported in Fig. 13.

We find that the values of precision, recall, and F-measure show decreasing trends with increasing E_Y for all three of these methods. As $E_Y \leq 10$, all measures of coif1MF have remained approximately constant and remain at a higher level than other methods. However, the recalls of DFT and TM are easily affected by E_Y because only the 1-D information along the x-axis direction is useful for WTMF methods, while the structure along the x-axis direction in the texture region is hardly

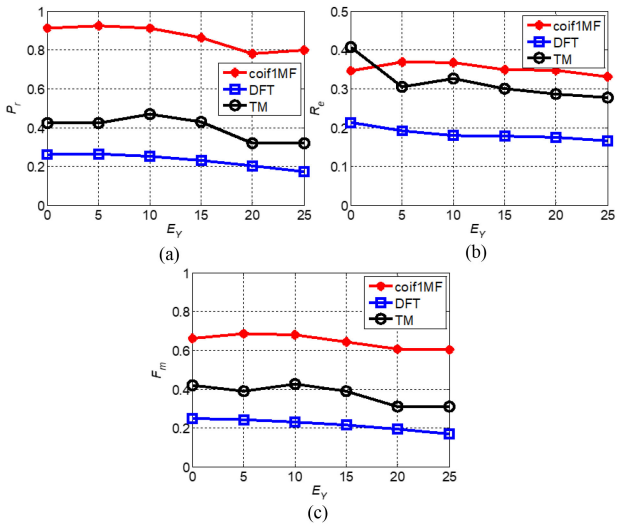

Fig. 13. Sensitivity of the texture region defect detection to localization error. (a) The curves of $P_r - E_y$. (b) The curves of $R_e - E_y$. (c) The curves of $F_m - E_y$.

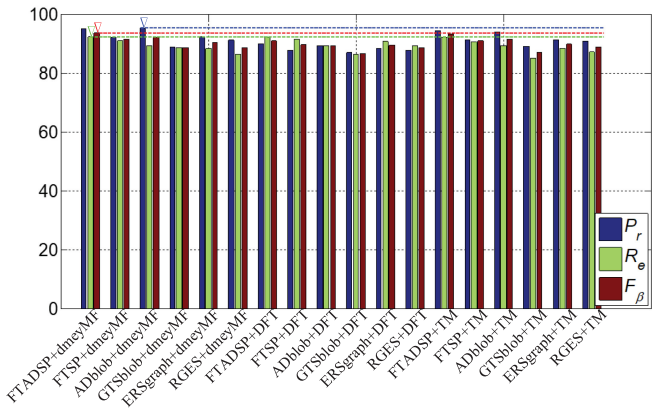

Fig. 14. Measures of the compared methods for the entire bottle bottom defect detection. The best results are marked by the "▽."

affected by the localization error. Unlike WTMF, the two other methods employ a 2-D structure of the bottom texture, which is sensitive to the localization precision.

F. Performance of the Entire Framework

To further evaluate the performances of all compared methods on the entire bottle bottom, the data set including 1230 bottom images is used for testing. Three methods, dmeyMF, DFT, and TM, and six approaches, FTADSP, FTSP, ADblob, GTSblob, ERSgraph, and RGES, are separately tested on the annular texture and central panel regions, respectively. Note that only FTSP is tested because it is superior to the other SMSP methods, and only dmeyMF is evaluated since all WTMF methods have similar performances. The parameter settings of FTADSP are $K = 400$, $T_{RG} = 10$, $T_{sm} = 65$, $T_{\text{area}} = 4$, and $T_{AD} = 12$. The quantitative indices are reported in Fig. 14.

It is clear that the proposed FTADSP+dmeyMF combination method is better than any other combinations, i.e., $P_r = 95.00\%$, $R_e = 92.10\%$, and $F_\beta = 93.55\%$, where the latter two evaluation indicators have achieved the corresponding best results. For precision, ADblob+dmeyMF achieves the best result, 95.10%, while the precision of FTADSP+dmeyMF is only 0.10% lower than that of ADblob+dmeyMF. The indices of the entire framework are clearly higher than those of the separate measurement regions because the FP and FN errors can be naturally eliminated for unqualified and qualified bottles, respectively. For example, if there are many defects for an unqualified bottle bottom, as long as one defect in any measurement region can be correctly detected, even if many normal regions are falsely detected as defects and many real defects cannot be accurately inspected, the final result of the entire bottom is still correct.

V. Further Discussion

Although we have tested the proposed framework under test condition, there are really still some deployment constrained questions in the future practical application that need to be considered.

1) The false detection may occur when the presented framework is applied, despite the robustness of our strategy being very strong for the same kind of the bottle bottom. Few other kinds of the bottle bottoms may exist in the practical production line, although this phenomenon is rare. For each type of bottom, defects can be detected accurately only when the parameter setting is proper, while the in-line parameter setting is impossible to realize in the production processing. Hence, it is necessary to study the abnormal type detection of bottles.
2) For the proposed framework, there are still some problems, such as many parameters need to be set manually, which is time-consuming. In the future, we will further improve the framework in two aspects. First, we will combine machine learning methods with our framework for reducing the number of parameters and improving the detection accuracy. Second, we will implement WTMF methods with C++ language and improve the superpixel segmentation algorithm to further speed up.

VI. Conclusion

In this article, a surface defect detection framework for glass bottle bottom using visual attention model and wavelet transform was proposed and tested on four data sets, which are acquired by our designed vision system. The main research work is summarized as follows.

1) The ERSCD strategy was proposed to localize the ROI of the testing bottle bottom, and the ROI was then divided into the central panel region and annular texture region.
2) The FTADSP method, which integrates saliency detection, anisotropic diffusion, and an improved superpixel segmentation, was proposed to detect defects in the central panel region.
3) The WTMF strategy, which combines wavelet transform with multiscale filtering, was proposed for the annular texture region defect detection.
4) The proposed framework was implemented and tested on our designed vision system. Many visual attention models, wavelet transform with different wavelet functions,

and conventional methods were evaluated on four data sets acquired with the designed apparatus. The precision and recall of the proposed framework were 95.00% and 92.10%, respectively. The average consumed time of our framework is about 535 ms. The experimental results show that the proposed methods can achieve the best performances compared with many other traditional approaches.

It is also believed that ERSCD can be used for general single circular object detection; that FTADSP can be applied in general for the inspection of arbitrary low-contrast, nonuniform light transmission or illumination surfaces; and that WTMF can be employed for object detection in strip texture images. These topics are worthy of further investigation.

References

[1] H. Liu, Y. Wang, and F. Duan, "An empty bottle intelligent inspector based on support vector machines and fuzzy theory," in *Proc. 6th World Congr. Intell. Control Autom.*, Jun. 2006, pp. 9739–9743.

[2] Y. Li, Y. F. Li, Q. L. Wang, D. Xu, and M. Tan, "Measurement and defect detection of the weld bead based on online vision inspection," *IEEE Trans. Instrum. Meas.*, vol. 59, no. 7, pp. 1841–1849, Jul. 2010.

[3] H. Yang, K. Song, S. Mei, and Z. Yin, "An accurate mura defect vision inspection method using outlier-prejudging-based image background construction and region-gradient-based level set," *IEEE Trans. Autom. Sci. Eng.*, vol. 15, no. 4, pp. 1704–1721, Oct. 2018.

[4] C. Jian, J. Gao, and Y. Ao, "Automatic surface defect detection for mobile phone screen glass based on machine vision," *Appl. Soft Comput.*, vol. 52, pp. 348–358, Mar. 2017.

[5] H. Zhang, X. Jin, Q. M. J. Wu, Y. Wang, Z. He, and Y. Yang, "Automatic visual detection system of railway surface defects with curvature filter and improved Gaussian mixture model," *IEEE Trans. Instrum. Meas.*, vol. 67, no. 7, pp. 1593–1608, Jul. 2018.

[6] H. Wang, J. Zhang, Y. Tian, H. Chen, H. X. Sun, and K. Liu, "A simple guidance template-based defect detection method for strip steel surfaces," *IEEE Trans. Ind. Informat.*, vol. 15, no. 5, pp. 2798–2809, May 2019.

[7] M. Win, A. R. Bushroa, M. A. Hassan, N. M. Hilman, and A. Ide-Ektessabi, "A contrast adjustment thresholding method for surface defect detection based on mesoscopy," *IEEE Trans. Ind. Informat.*, vol. 11, no. 3, pp. 642–649, Jun. 2015.

[8] D. M. Tsai and J. Y. Luo, "Mean shift-based defect detection in multicrystalline solar wafer surfaces," *IEEE Trans. Ind. Informat.*, vol. 7, no. 1, pp. 125–135, Feb. 2011.

[9] J. Ge *et al.*, "A system for automated detection of ampoule injection impurities," *IEEE Trans. Autom. Sci. Eng.*, vol. 14, no. 2, pp. 1119–1128, Apr. 2017.

[10] H. Zhang *et al.*, "Automated machine vision system for liquid particle inspection of pharmaceutical injection," *IEEE Trans. Instrum. Meas.*, vol. 67, no. 6, pp. 1278–1297, Jun. 2018.

[11] F. Shafait, S. M. Imran, and S. Klette-Matzat, "Fault detection and localization in empty water bottles through machine vision," in *Proc. E-Tech*, Jul. 2004, pp. 30–34.

[12] F. Duan, Y. N. Wang, H. J. Liu, and Y. G. Li, "A machine vision inspector for beer bottle," *Eng. Appl. Artif. Intell.*, vol. 20, no. 7, pp. 1013–1021, Oct. 2007.

[13] S. Ma, B. Huang, H. Wang, and J. Guo, "Algorithm research on location of bottle mouth and bottom in intelligent empty bottle inspection system," in *Proc. IEEE Int. Conf. Autom. Logistics*, Aug. 2009, pp. 819–824.

[14] B. Huang, S. Ma, Y. Lv, H. Zhang, C. Liu, and H. Wang, "Research on bottom detection in intelligent empty bottle inspection system," *Indonesian J. Elect. Eng. Comput. Sci.*, vol. 11, no. 10, pp. 5571–5578, Oct. 2013.

[15] B. Huang *et al.*, "Research and implementation of machine vision technologies for empty bottle inspection systems," *Eng. Sci. Technol. Int. J.*, vol. 21, no. 1, pp. 159–169, Feb. 2018.

[16] X. Zhou *et al.*, "Automated visual inspection of glass bottle bottom with saliency detection and template matching," *IEEE Trans. Instrum. Meas.*, to be published, doi: 10.1109/TIM.2018.2886977.

[17] R. O. Duda and P. E. Hart, "Use of the hough transform to detect lines and curves in pictures," *Commun. ACM*, vol. 15, no. 1, pp. 11–15, Jan. 1972.

[18] S. M. Chao and D. M. Tsai, "Anisotropic diffusion with generalized diffusion coefficient function for defect detection in low-contrast surface images," *Pattern Recognit.*, vol. 43, no. 5, pp. 1917–1931, May 2010.

[19] C. S. Chen, C. M. Weng, and C. C. Tseng, "An efficient detection algorithm based on anisotropic diffusion for low-contrast defect," *Int. J. Adv. Manuf. Technol.*, vol. 94, nos. 9–12, pp. 4427–4449, Feb. 2018.

[20] Z. He, Y. Wang, F. Yin, and J. Liu, "Surface defect detection for high-speed rails using an inverse P-M diffusion model," *Sensor Rev.*, vol. 36, no. 1, pp. 86–97, Jan. 2016.

[21] X. Bai, Y. Fang, W. Lin, L. Wang, and B.-F. Ju, "Saliency-based defect detection in industrial images by using phase spectrum," *IEEE Trans. Ind. Informat.*, vol. 10, no. 4, pp. 2135–2145, Nov. 2014.

[22] T. Chen, Y. Wang, C. Xiao, and Q. M. J. Wu, "A machine vision apparatus and method for can-end inspection," *IEEE Trans. Instrum. Meas.*, vol. 65, no. 9, pp. 2055–2066, Sep. 2016.

[23] M. Y. Liu, O. Tuzel, S. Ramalingam, and R. Chellappa, "Entropy rate superpixel segmentation," in *Proc. IEEE Conf. Comput. Vis. Pattern Recog.*, Jun. 2011, pp. 2097–2104.

[24] I. Kasa, "A curve fitting procedure and its error analysis," *IEEE Trans. Instrum. Meas.*, vol. IM-25, no. 1, pp. 8–14, Mar. 1976.

[25] T. C. Chen and K. L. Chung, "An efficient randomized algorithm for detecting circles," *Comput. Vis. Image Understanding*, vol. 83, no. 2, pp. 172–191, Aug. 2001.

[26] L. Itti, C. Koch, and E. Niebur, "A model of saliency-based visual attention for rapid scene analysis," *IEEE Trans. Pattern Anal. Mach. Intell.*, vol. 20, no. 11, pp. 1254–1259, Nov. 1998.

[27] G. Li, J. Shi, H. Luo, and M. Tang, "A computational model of vision attention for inspection of surface quality in production line," *Mach. Vis. Appl.*, vol. 24, no. 4, pp. 835–844, Jul. 2013.

[28] R. Achantay, S. Hemamiz, F. Estraday, and S. Ssstrunky, "Frequency-tuned salient region detection," in *Proc. IEEE Conf. Comput. Vis. Pattern Recog.*, Jun. 2009, pp. 1597–1604.

[29] X. Zhou, Y. Wang, Q. Zhu, C. Xiao, and X. Lu, "SSG: Superpixel segmentation and grabcut-based salient object segmentation," *Vis. Comput.*, vol. 35, no. 3, pp. 385–398, Mar. 2019.

[30] C. Lorenz, I. C. Carlsen, T. M. Buzug, C. Fassnacht, and J. Weese, "Multi-scale line segmentation with automatic estimation of width, contrast and tangential direction in 2D and 3D medical images," in *Proc. CVRMed-MRCAS*, 1997, pp. 233–242.

[31] S. G. Mallat, "A theory for multiresolution signal decomposition: the wavelet representation," *IEEE Trans. Pattern Anal. Mach. Intell.*, vol. 11, no. 7, pp. 674–693, Jul. 1989.

[32] H. K. Yuen, J. Princen, J. Illingworth, and J. Kittler, "Comparative study of hough transform methods for circle finding," *Image Vis. Comput.*, vol. 8, no. 1, pp. 71–77, Feb. 1990.

[33] Z. Yun and M. Shah, "Visual attention detection in video sequences using spatiotemporal cues," in *Proc. 14th ACM Int. Conf. Multimedia*, Oct. 2006, pp. 815–824.

[34] M. M. Cheng, N. J. Mitra, X. Huang, P. H. Torr, and S. M. Hu, "Global contrast based salient region detection," *IEEE Trans. Pattern Anal. Mach. Intell.*, vol. 37, no. 3, pp. 569–582, Mar. 2015.

[35] X. Hou and L. Zhang, "Saliency detection: A spectral residual approach," in *Proc. IEEE Conf. Comput. Vis. Pattern Recog.*, Jun. 2007, pp. 1–8.

[36] G. Yildirim and S. Ssstrunk, "FASA: Fast, accurate, and size-aware salient object detection," in *Proc. Asian Conf. Comput. Vis.*, Nov. 2014, pp. 514–528.

Xianen Zhou received the B.S. degree in electronic information engineering from the Hunan University of Science and Engineering, Yongzhou, China, in 2010, and the M.S. degree in circuits and systems from the East China University of Technology, Nanchang, China, in 2013. He is currently working toward the Ph.D. degree in pattern recognition and intelligent system with Hunan University, Changsha, China.

His current research interests include machine vision, machine learning, and automatic visual detection systems.

Yaonan Wang received the B.S. degree in computer engineering from the East China University of Technology, Fuzhou, China, in 1981, and the M.S. and Ph.D. degrees in electrical engineering from Hunan University, Changsha, China, in 1990 and 1994, respectively.

From 1998 to 2000, he was a Senior Humboldt Fellow in Germany, and from 2001 to 2004, he was a Visiting Professor with the University of Bremen, Bremen, Germany. Since 1995, he has been a Professor with the College of Electrical and Information Engineering, Hunan University. His current research interests include intelligent control and machine vision systems for industrial applications.

Qing Zhu received the B.S., M.S., and Ph.D. degrees in electrical engineering from Hunan University, Changsha, China, in 1989, 2000, and 2008, respectively.

She is currently an Associate Professor and a Ph.D. Supervisor with the College of Electrical and Information Engineering, Hunan University. Her current research interests include image processing and communication technology.

Jianxu Mao received the B.S. degree in computer application from Nanchang University, Nanchang, China, in 1993, the M.S. degree in earth exploration and information technology from the East China Institute of Technology, Fuzhou, China, in 1999, and the Ph.D. degree in control theory and control engineering from Hunan University, Changsha, China, in 2003.

From 1993 to 1999, he was with the East China Institute of Technology. Since 2005, he has been an Associate Professor with the College of Electrical and Information Engineering, Hunan University. His current research interests include image processing, pattern recognition, and intelligent information processing.

Changyan Xiao received the B.E. and M.S. degrees in mechanical and electronic engineering from the National University of Defense Technology, Changsha, China, in 1994 and 1997, respectively, and the Ph.D. degree in biomedical engineering from Shanghai Jiaotong University, Shanghai, China, in 2005.

From 2008 to 2009, he was a Visiting Postdoctoral Researcher with the Division of Image Processing, Leiden University Medical Center, Leiden, Netherlands. Since 2005, he has been an Associate Professor and a Full Professor with the College of Electrical and Information Engineering, Hunan University, Changsha. His current research interests include medical imaging and machine vision.

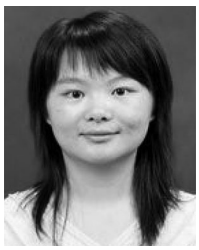

Xiao Lu received the B.E. degree from Hunan University, Changsha, China, in 2007, the M.S. degree from Southeast University, Nanjing, China, in 2010, and the Ph.D. degree from Hunan University in 2016, all in electrical engineering.

She is currently an Associate Professor with the College of Engineering and Design, Hunan Normal University, Changsha. Her current research interests include machine vision, pattern recognition, and machine learning.

Hui Zhang received the B.S., M.S., and Ph.D. degrees in pattern recognition and intelligent system from Hunan University, Changsha, China, in 2004, 2007, and 2012, respectively.

He is currently an Assistant Professor with the College of Electrical and Information Engineering, Changsha University of Science and Technology, Changsha. His current research interests include machine vision, sparse representation, and visual tracking.